Dirac solitons and topological edge states in the β-Fermi-Pasta-Ulam-Tsingou dimer lattice

Rajesh Chaunsali [1,*], Panayotis G. Kevrekidis [2], Dimitri Frantzeskakis [3], and Georgios Theocharis [4,†]

[1]*Department of Aerospace Engineering, Indian Institute of Science, Bangalore 560012, India*
[2]*Department of Mathematics and Statistics, University of Massachusetts, Amherst, Massachusetts 01003-4515, USA*
[3]*Department of Physics, National and Kapodistrian University of Athens, Panepistimiopolis, Zografos, Athens 15784, Greece*
[4]*LAUM, UMR No. 6613, CNRS, Le Mans Université, Avenue Olivier Messiaen, 72085 Le Mans, France*

We consider a dimer lattice of the Fermi-Pasta-Ulam-Tsingou (FPUT) type, where alternating linear couplings have a controllably small difference and the cubic nonlinearity (β-FPUT) is the same for all interaction pairs. We use a weakly nonlinear formal reduction within the lattice band gap to obtain a continuum, nonlinear Dirac-type system. We derive the Dirac soliton profiles and the model's conservation laws analytically. We then examine the cases of the semi-infinite and the finite domains and illustrate how the soliton solutions of the bulk problem can be glued to the boundaries for different types of boundary conditions. We thus explain the existence of various kinds of nonlinear edge states in the system, of which only one leads to the standard topological edge states observed in the linear limit. We finally examine the stability of bulk and edge states and verify them through direct numerical simulations, in which we observe a solitonlike wave setting into motion due to the instability.

I. INTRODUCTION

The study of systems of the Fermi-Pasta-Ulam-Tsingou (FPUT) type [1] has an exciting and long history within nonlinear science [2]. More recently, the relevant topics received substantial attention due to experimental connections [3]. For instance, granular crystals have offered a reasonably mature platform where various nonlinear phenomena are explored, e.g., solitons, discrete breathers, and dispersive shock dynamics [4–7]. Additionally, diverse platforms based on magnets [8,9] and origami cells [10] have also been considered.

On the other hand, the exploration of nonlinear partial differential equations (PDEs) of the Dirac type has also recently gained considerable traction. This is due to the emergence of such equations for boson gases confined in honeycomb lattices [11,12] and light propagation in photorefractive honeycomb lattices [13,14]; the latter theme has allowed for the observation of key features such as conical diffraction, among others. These efforts have led to a wide range of mathematical works devoted to studying solitary waves and their stability in such systems [15,16].

Furthermore, the third axis of problems with substantial research activity has been band topology and its potential impact on designing new materials and structures for various engineering applications. Relevant studies range from the fundamental properties of electronic materials [17] to the engineering of optical lattices in cold-atom systems [18] and from topological photonics [19] to applications in phononic and acoustic systems [20,21]. A central role in such works has been played by the so-called bulk-boundary correspondence [22]. This has enabled an understanding (based on infinite or bulk materials) of how finite or semi-infinite systems may behave in the presence of corners, edges, and surfaces [23–25].

The present work treads at the nexus of all three above directions. In particular, we aim to examine a dimer system of the FPUT type. Exponentially localized in space, periodic in time solutions in the form of the so-called discrete breathers [26,27] have been identified in such systems in several earlier works [28–30]. Typically, in such problems, a variation of the mass between the elements of the dimer lattice is considered. Here, however, we consider a model in the spirit of numerous works motivated by the so-called Su-Schrieffer-Heeger (SSH) model [31], a recent popular platform for controlling the band-gap features and associated edge modes [19]. More concretely, we explore a dimer in the linear couplings [32,33] while we preserve the softening nonlinearity of the same (β-FPUT type) across all the bonds (intersite) of the lattice. It is worth noting that a very similar linear setting, but for an on-site (rather than intersite) nonlinearity, has been very recently explored in Ref. [34]. This work aims to provide an analysis (using both continuum methods and direct numerical simulations) of the prototypical nonlinear patterns that can arise in bulk and the edges of the nonlinear lattice model under consideration.

Our presentation is structured as follows. Section II introduces the model and briefly discusses its properties in the linear regime. In Sec. III, by leveraging a formal continuum limit, we are led naturally to a nonlinear Dirac equation. We find that the nonlinearity of the derived Dirac model does not match well-established cases, such as the Soler (Gross-Neveu) or the (integrable) massive Thirring model [15,16]. Nevertheless, inspired by related work, such as that of Ref. [35], we devise a sequence of linear and nonlinear transformations that ultimately allows us to compute the stationary soliton of the continuum approximation. Part of our motivation for developing the relevant reduction stems from the existence of

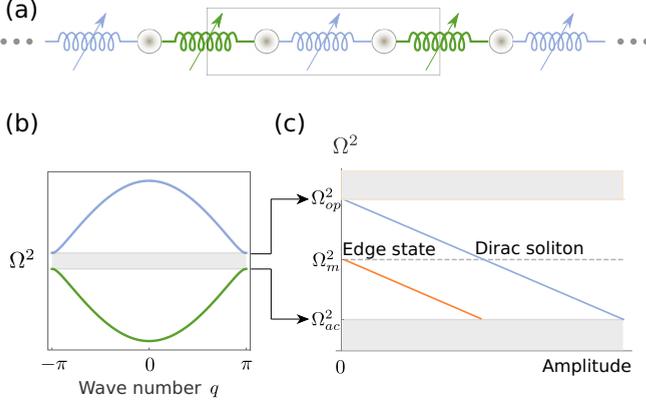*rchaunsali@iisc.ac.in
†georgios.theocharis@univ-lemans.fr

FIG. 1. (a) FPUT dimer lattice with equal masses connected with nonlinear springs with two different linear stiffnesses. The box denotes the unit cell. (b) Dispersion diagram of the linear system (i.e., when the nonlinear coefficient $\Gamma = 0$). (c) Schematic of the amplitude-dependent edge state and the Dirac soliton residing inside the band gap.

established stability criteria for PDEs of the nonlinear Dirac type [36] that we intend to leverage to suggest the stability of the identified waveforms. In Sec. IV we explore how to adapt the relevant solutions to the context of a semi-infinite (i.e., with one end being bounded) continuum. In Sec. V we analyze the nonlinear solutions in the bulk and edges of the finite lattice and compare them with ones obtained from solving the PDEs. In Sec. VI we summarize our findings and present some exciting directions for future studies. The Appendices complement our presentation with some of the technical details of the system.

II. MODEL SETUP

We consider a periodic chain made of two alternating springs with a weak cubic nonlinearity, as shown in Fig. 1(a). The nondimensional equations of motion for the two particles inside the nth unit cell can be written as follows [37]:

$$\ddot{\xi}_{1,n} = (1+\gamma)(\xi_{2,n-1} - \xi_{1,n}) + \Gamma(\xi_{2,n-1} - \xi_{1,n})^3$$
$$- (1-\gamma)(\xi_{1,n} - \xi_{2,n}) - \Gamma(\xi_{1,n} - \xi_{2,n})^3,$$
$$\ddot{\xi}_{2,n} = (1-\gamma)(\xi_{1,n} - \xi_{2,n}) + \Gamma(\xi_{1,n} - \xi_{2,n})^3$$
$$- (1+\gamma)(\xi_{2,n} - \xi_{1,n+1}) - \Gamma(\xi_{2,n} - \xi_{1,n+1})^3. \quad (1)$$

Here $\xi_{m,n}$ denotes the normalized displacement of the mth particle inside the nth cell, $1-\gamma$ and $1+\gamma$ represent the linearized stiffnesses of two springs, and Γ is the nonlinearity parameter. We take the same nonlinearity parameter for all springs to make the analytical treatment simpler.

In the linear limit ($\Gamma \to 0$), the system represents a periodic chain consisting of two alternating springs with stiffnesses $1-\gamma$ and $1+\gamma$. The dispersion relation has two branches as shown in Fig. 1(b). By assuming $\gamma > 0$, at the edge of Brillouin zone, i.e., at wave number $q = \pm\pi$, the acoustic (lower) and optical (upper) cutoff frequencies are given by

$$\Omega_{\text{ac}}^2 = 2(1-\gamma), \quad \Omega_{\text{op}}^2 = 2(1+\gamma),$$

respectively. Thus, the dispersion curve has a band gap (defined in terms of the squared frequency here) of width $\Omega_{\text{op}}^2 - \Omega_{\text{ac}}^2$. Moreover, the eigenmode corresponding to Ω_{ac}^2 is given by

$$(\xi_{1,n}, \xi_{2,n}) = (A, -A)\exp(iqn) = (-1)^n(A, -A),$$

where A is the amplitude of oscillation. Physically, this means that the two particles inside the unit cell oscillate out of phase. Similarly, the eigenmode at Ω_{op}^2 is given by

$$(\xi_{1,n}, \xi_{2,n}) = (A, A)\exp(iqn) = (-1)^n(A, A),$$

representing the in-phase motion of particles inside the unit cell. The prefactor $(-1)^n$ is due to the corresponding wave number. We will utilize these characteristics to discover amplitude-dependent solitons and edge states residing in this band gap, as illustrated in Fig. 1(c). Having set up the relevant model, we now turn to the analysis of its prototypical soliton solutions over the infinite lattice.

III. INFINITE CONTINUUM

We focus on the weakly nonlinear wave solutions, i.e., $\Gamma = \epsilon_1 \tilde{\Gamma}$ with $\epsilon_1 \ll 1$, inside the band gap for the wave number $q = \pi$. Moreover, we consider a small band gap such that $\gamma = \epsilon_2 \tilde{\gamma}$ with $\epsilon_2 \ll 1$. We further assume that nonlinearity and band gap are of the same order, i.e., $\epsilon_1 = \epsilon_2 = \epsilon$. We then look for slowly varying solutions around frequency Ω. The structure of the two eigenmodes at $q = \pi$ suggests that we look for solutions with the ansatz

$$\xi_{1,n} = \frac{(-1)^n}{2}[u(z,\tau)\exp(i\Omega t) + u^*(z,\tau)\exp(-i\Omega t)],$$
$$\xi_{2,n} = \frac{(-1)^n}{2}[v(z,\tau)\exp(i\Omega t) + v^*(z,\tau)\exp(-i\Omega t)], \quad (2)$$

where the asterisk denotes complex conjugate, $z = \epsilon n$, and $\tau = \epsilon t$. We substitute the ansatz in Eq. (1) and proceed formally to a continuum approximation; note that, to do so, we are partly motivated by its successes in similar problems [38,39] and partly through an *a posteriori* comparison with the lattice dynamical results. We thus consider that the functions u and v are approximated by continuous functions of the position (and time), and expanding in the Taylor series, we equate the various orders of ϵ.

At $O(\epsilon^0)$, we obtain $\Omega = \sqrt{2}$. In the dimer model presented in Sec. II, this frequency corresponds to the midgap frequency $\Omega_m = \sqrt{(\Omega_{\text{ac}}^2 + \Omega_{\text{op}}^2)/2} = \sqrt{2}$. This makes sense because as the stiffness difference γ approaches zero (the leading-order dynamics), the band gap in our dimer lattice goes to the limit of the monatomic lattice with frequency $\Omega = \sqrt{2}$ at $q = \pi$.

At $O(\epsilon^1)$, however, we obtain the following system of nonlinear PDEs for the solutions around $\Omega_m = \sqrt{2}$:

$$-4i\sqrt{2}\frac{\partial u(z,\tau)}{\partial \tau} = -2\frac{\partial v(z,\tau)}{\partial z} + 4\tilde{\gamma}v(z,\tau)$$
$$+ 3\tilde{\Gamma}[|u(z,\tau)|^2 + 2|v(z,\tau)|^2]u(z,\tau)$$
$$+ 3\tilde{\Gamma}v(z,\tau)^2u^*(z,\tau),$$

$$-4i\sqrt{2}\frac{\partial v(z,\tau)}{\partial \tau} = 2\frac{\partial u(z,\tau)}{\partial z} + 4\tilde{\gamma}u(z,\tau)$$
$$+ 3\tilde{\Gamma}[2|u(z,\tau)|^2 + |v(z,\tau)|^2]v(z,\tau)$$
$$+ 3\tilde{\Gamma}u(z,\tau)^2 v^*(z,\tau). \tag{3}$$

In the linear limit $\tilde{\Gamma} \to 0$, these PDEs closely follow the dispersion curve obtained for the discrete lattice in Eq. (1) (see Appendix A for comparison). Interestingly, we can further simplify these PDEs using a suitable rotation (together with a simple rescaling) and obtain a bispinor nonlinear Dirac (NLD) equation in the form

$$i\frac{\partial \psi_1}{\partial \tau} = -\frac{\partial \psi_2}{\partial s} - \tilde{M}\psi_1 + |\psi_1|^2\psi_1,$$
$$i\frac{\partial \psi_2}{\partial \tau} = \frac{\partial \psi_1}{\partial s} + \tilde{M}\psi_2 + |\psi_2|^2\psi_2. \tag{4}$$

Here $\psi_1 = \tilde{G}(u+v)$, $\psi_2 = \tilde{G}(u-v)$, $\tilde{G} = \sqrt{-3\tilde{\Gamma}/4\sqrt{2}}$, $s = 2\sqrt{2}z$, $\tilde{M} = \tilde{\gamma}/\sqrt{2}$. We consider $\tilde{\Gamma} < 0$ for the softening nonlinearity of interest herein. Also, the tilde indicates the normalized system parameters of $O(1)$. It is worth pointing out that these equations are invariant under the transformation $s \to -s$, $\psi_1 \to \psi_1$, and $\psi_2 \to -\psi_2$. Therefore, if the initial conditions of the PDEs $\psi_1(s)$ and $\psi_2(s)$ are even and odd functions of s, respectively, the solution would preserve this symmetry for all times. It is relevant to point out here that the presence of nonlinearities involving self- and cross-phase modulation (in the language of nonlinear optics) precludes the existence of Lorentz invariance in the model derived herein, contrary, e.g., to what is the case in the setting discussed in [40]. Note that the same procedure can be used to obtain the NLD equations for the Klein-Gordon lattice with the on-site nonlinearity. The latter model has been explored in considerable detail in the very recent work [34].

It is worth mentioning some key differences between this system and the dimer models, in which the envelope dynamics inside the band gap is governed by the nonlinear Schrodinger (NLS) equation [41]. In fact, the latter is the case with a large band gap $\gamma \approx O(1)$ and weaker nonlinearity $\Gamma \approx O(\epsilon^2)$, where the slow scales $z = \epsilon n$ and $\tau = \epsilon^2 t$ govern the envelope solutions. However, it was shown by Hu et al. [42] that a small band gap, as is the case here, could lead to new kinds of gap solutions governed by coupled-mode equations [43].

Next, following Ref. [35], we further employ the transformations

$$\psi_1 \to (\psi_a + \psi_b)e^{i\tilde{\omega}\tau}, \quad \psi_2 \to -i(\psi_a - \psi_b)e^{i\tilde{\omega}\tau}$$

and obtain

$$\frac{\partial \psi_a}{\partial \tau} = \frac{\partial \psi_a}{\partial s} - i\tilde{\omega}\psi_a + i\tilde{M}\psi_b$$
$$- i(|\psi_a|^2 + |\psi_b|^2)\psi_a - i(\psi_a\psi_b^* + \psi_a^*\psi_b)\psi_b,$$
$$\frac{\partial \psi_b}{\partial \tau} = -\frac{\partial \psi_b}{\partial s} + i\tilde{M}\psi_a - i\tilde{\omega}\psi_b$$
$$- i(|\psi_a|^2 + |\psi_b|^2)\psi_b - i(\psi_a\psi_b^* + \psi_a^*\psi_b)\psi_a, \tag{5}$$

where $\tilde{\omega}$ can be interpreted as the frequency offset from the midgap frequency Ω_m. The band-gap region corresponds to

$\tilde{\omega} \in [-\tilde{M}, \tilde{M}]$. It is relevant to point out here that the resulting class of models of Eq. (5) is strongly reminiscent of the one describing the propagation of slow Bragg solitons in nonlinear refractive periodic media; these models were widely studied over 30 years ago in pioneering studies such as those in [44,45]. We will leverage techniques for identification of the solitons in such systems to obtain exact solutions for the stationary waveforms in what follows.

A. Stationary solutions

We now seek stationary solutions for $\tilde{\omega}$, which corresponds to a frequency $\Omega = \Omega_m + \epsilon\tilde{\omega}$ in the dispersion diagram. Such stationary solutions do not depend on time and hence Eq. (5) is reduced to the form

$$\frac{d\psi_a}{ds} = i[\tilde{\omega}\psi_a - \tilde{M}\psi_b + (|\psi_a|^2 + |\psi_b|^2)\psi_a$$
$$+ (\psi_a\psi_b^* + \psi_a^*\psi_b)\psi_b],$$
$$\frac{d\psi_b}{ds} = i[\tilde{M}\psi_a - \tilde{\omega}\psi_b - (|\psi_a|^2 + |\psi_b|^2)\psi_b$$
$$- (\psi_a\psi_b^* + \psi_a^*\psi_b)\psi_a]. \tag{6}$$

Next we use a polar decomposition into amplitude and phase variables, namely,

$$\psi_a(s) = \phi_a(s)\exp\{i[\theta_0(s) + \theta(s)]/2\},$$
$$\psi_b(s) = \phi_b(s)\exp\{i[\theta_0(s) - \theta(s)]/2\},$$

with $\phi_a(s), \phi_b(s) \geqslant 0$, and arrive at the following four coupled ordinary differential equations (ODEs) for $\phi_a(s)$, $\phi_b(s)$, $\theta_0(s)$, and $\theta(s)$:

$$\frac{d\phi_a}{ds} = \phi_b \sin\theta(2\phi_a\phi_b\cos\theta - \tilde{M}), \tag{7}$$

$$\frac{d\phi_b}{ds} = \phi_a \sin\theta(2\phi_a\phi_b\cos\theta - \tilde{M}), \tag{8}$$

$$\frac{d\theta}{ds} = 2\tilde{\omega} + \left(\frac{\phi_a}{\phi_b} + \frac{\phi_b}{\phi_a}\right) \tag{9}$$

$$\times [\cos\theta(2\phi_a\phi_b\cos\theta - \tilde{M}) + 2\phi_a\phi_b], \tag{10}$$

$$\frac{d\theta_0}{ds} = \left(\frac{\phi_a}{\phi_b} - \frac{\phi_b}{\phi_a}\right)[\cos\theta(\tilde{M} - 2\phi_a\phi_b\cos\theta)]. \tag{11}$$

By dividing Eq. (7) by Eq. (8) we get

$$\frac{d\phi_a}{d\phi_b} = \frac{\phi_b}{\phi_a}, \tag{12}$$

which upon integration yields

$$\phi_a^2 - \phi_b^2 = c. \tag{13}$$

Here the integration constant c can be found from the boundary conditions.

B. Dirac soliton

In this study, we are interested in localized soliton solutions of this continuum approximation so that we could translate them into approximate solutions (or initial guesses in the context of our numerical computations) of the discrete system
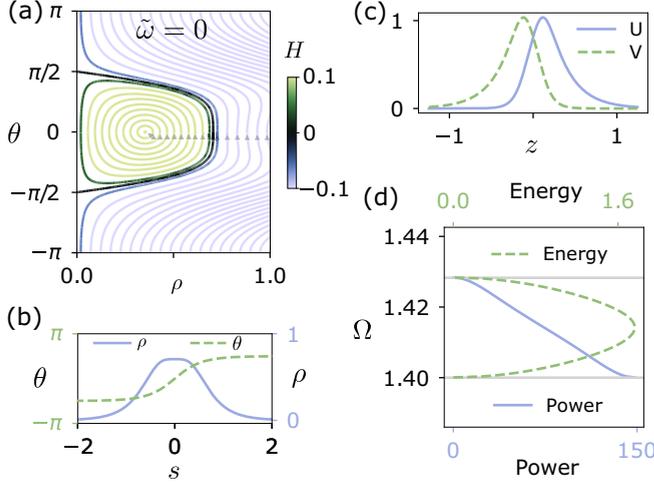
FIG. 2. Infinite continuum NLD findings. (a) Phase portrait for Eqs. (14) and (15) at $\tilde{\omega} = 0$. The colormap denotes the value of the Hamiltonian that corresponds to each trajectory. The heteroclinic orbit, which corresponds to $H = 0$, is shown with the black line. (b) Dirac soliton profile $(\rho(s), \theta(s))$ that corresponds to the heteroclinic orbit. (c) Dirac soliton profile $(U(z), V(z))$. (d) Energy and power, the conserved quantities of the NLD equation, obtained for the soliton solution inside the band gap.

breather waveforms. Therefore, we impose the boundary conditions $\phi_a(s) \to 0$ and $\phi_b(s) \to 0$ as $s \to \infty$. This translates into vanishing u, v, and ξ at infinity, and $c = 0$ from Eq. (13). Assuming $\phi_a(s)$ and $\phi_b(s)$ to be non-negative, we thus have $\phi_a(s) = \phi_b(s)$ for $s \in (-\infty, \infty)$. A solution decaying to zero also as $s \to -\infty$, e.g., a soliton,[1] naturally satisfies this condition. Further, since $c = 0$, we define $\rho \equiv \phi_a^2 = \phi_b^2$ and cast Eqs. (7)–(11) into the form

$$\frac{d\rho}{ds} = 2\rho \sin\theta (2\rho \cos\theta - \tilde{M}), \quad (14)$$

$$\frac{d\theta}{ds} = 2\cos\theta (2\rho \cos\theta - \tilde{M}) + 4\rho + 2\tilde{\omega}, \quad (15)$$

$$\frac{d\theta_0}{ds} = 0. \quad (16)$$

Equation (16) can readily be integrated, leading to $\theta_0(s) = c_1$. This implies that

$$\psi_a(s) = \sqrt{\rho(s)} \exp(ic_1/2) \exp[i\theta(s)/2],$$

$$\psi_b(s) = \sqrt{\rho(s)} \exp(ic_1/2) \exp[-i\theta(s)/2],$$

and thus in the NLD picture we have

$$\psi_1(s, \tau) = 2\sqrt{\rho(s)} \cos[\theta(s)/2] \exp[i(\tilde{\omega}\tau + c_1/2)],$$

$$\psi_2(s, \tau) = 2\sqrt{\rho(s)} \sin[\theta(s)/2] \exp[i(\tilde{\omega}\tau + c_1/2)].$$

In what follows, we choose $c_1 = 0$ for simplicity, leveraging the (overall) gauge invariance of the equations.

---

[1] It should be understood here that the term soliton is used in a looser sense in which it describes spatially localized waveforms (rather than the narrower meaning of a solution of an integrable nonlinear partial differential equation).

The remaining two equations [Eqs. (14) and (15)] in ρ and θ are decoupled from the third. Therefore, to get better insight, we plot a two-dimensional (2D) phase portrait for these equations in Fig. 2(a) at a prototypical frequency ($\tilde{\omega} = 0$ representing the middle of the gap). We choose $\gamma = \Gamma = 0.02$ for all the studies hereafter, which translates to $\epsilon = 0.01$ and $\tilde{\gamma} = \tilde{\Gamma} = 2$. The phase portrait has a number of fixed points, including the two saddles at $(\rho, \theta) = (0, \pm\pi/2)$. Furthermore, to analytically track the solutions, Eqs. (14) and (15) can be seen as a dynamical system with the Hamiltonian

$$H(\rho, \theta) = -2\tilde{\omega}\rho - 2\rho^2 + 2\tilde{M}\rho \cos\theta - 2\rho^2 \cos^2\theta. \quad (17)$$

Since we are looking for a localized solution, i.e., $\rho \to 0$ for $s \to \pm\infty$, this solution is represented by the heteroclinic orbit, namely, the trajectory that connects the two saddle points for which $\rho = 0$. The corresponding value of the Hamiltonian for this trajectory is zero, $H = 0$. We thus obtain

$$\rho = \frac{\tilde{M}\cos\theta - \tilde{\omega}}{1 + \cos^2\theta}, \quad (18)$$

which we substitute in Eq. (15) to get

$$\frac{d\theta}{ds} = 2(\tilde{M}\cos\theta - \tilde{\omega}). \quad (19)$$

By integrating we obtain

$$\theta(s) = 2\tan^{-1}\left(\frac{\tilde{M} - \tilde{\omega}}{\sqrt{\tilde{M}^2 - \tilde{\omega}^2}} \tanh\left[\sqrt{\tilde{M}^2 - \tilde{\omega}^2}(s - s_0)\right]\right). \quad (20)$$

Here s_0 is the constant of integration. For the soliton solutions in the domain $s \in (-\infty, \infty)$, we can choose any s_0 because those represent shifted members of the family of solitons (rendered possible due to the translational invariance of the underlying model). For convenience, we choose a soliton centered at $s = 0$; therefore,

$$\theta(s) = 2\tan^{-1}\left(\frac{\tilde{M} - \tilde{\omega}}{\sqrt{\tilde{M}^2 - \tilde{\omega}^2}} \tanh\left[\sqrt{\tilde{M}^2 - \tilde{\omega}^2}s\right]\right). \quad (21)$$

In Fig. 2(b) we show the soliton profile. We note that the amplitude vanishes as $s \to \pm\infty$. However, the phase reverses from $-\pi/2$ to $\pi/2$. The latter indicates its similarity to a topological soliton.

Finally, $\rho(s)$ and $\theta(s)$ can be used to obtain

$$\psi_a(s) = \sqrt{\rho(s)} \exp[i\theta(s)/2], \quad (22)$$

$$\psi_b(s) = \sqrt{\rho(s)} \exp[-i\theta(s)/2], \quad (23)$$

$$\psi_1(s, \tau) = 2\sqrt{\rho(s)} \cos[\theta(s)/2] \exp(i\tilde{\omega}\tau), \quad (24)$$

$$\psi_2(s, \tau) = 2\sqrt{\rho(s)} \sin[\theta(s)/2] \exp(i\tilde{\omega}\tau), \quad (25)$$

$$u(z, \tau) = U(z) \exp(i\tilde{\omega}\tau), \quad (26)$$

$$v(z, \tau) = V(z) \exp(i\tilde{\omega}\tau), \quad (27)$$

where $s = 2\sqrt{2}z$ and

$$U(z) = \frac{\sqrt{2\rho(s)}}{\tilde{G}} \sin\left(\frac{\pi}{4} + \frac{\theta(s)}{2}\right),$$

$$V(z) = \frac{\sqrt{2\rho(s)}}{\tilde{G}} \sin\left(\frac{\pi}{4} - \frac{\theta(s)}{2}\right).$$

In Fig. 2(c) we show the soliton profile at $\tilde{\omega} = 0$ in terms of $U(z)$ and $V(z)$.

It is relevant to point out here (both for analytical and for numerical purposes) that it is possible to identify other trajectories of the dynamical system as well. In particular, a positive finite value of H leads to a quadratic equation for ρ that can be solved explicitly in terms of θ and back substituted into the ODE for $d\theta/ds$ in order to retrieve the corresponding periodic orbits from the integration of the ODE for $\theta = \theta(s)$.

C. Conserved quantities

We now discuss the frequency dependence of the conserved quantities of the NLD equations shown in Eq. (4). First, the power of the NLD equations is given as

$$P(\tilde{\omega}) = \left(\frac{1}{4G^2\sqrt{2}}\right)\int_{-\infty}^{\infty}(|\psi_1|^2 + |\psi_2|^2)\mathrm{d}s, \quad (28)$$

where the factor in front of the integration, which is independent of the frequency, is introduced to scale the expression and compare it with the total lattice energy of the stationary solutions of Eq. (1) (see Appendix B for details). For the stationary soliton [Eq. (21)], the power can thus be deduced to be

$$P(\tilde{\omega}) = \left(\frac{1}{2G^2}\right)\left[\tan^{-1}\left(1 + \sqrt{\frac{2(\tilde{M} - \tilde{\omega})}{\tilde{M} + \tilde{\omega}}}\right)\right.$$
$$\left. - \tan^{-1}\left(1 - \sqrt{\frac{2(\tilde{M} - \tilde{\omega})}{\tilde{M} + \tilde{\omega}}}\right)\right], \quad (29)$$

where $G^2 = \epsilon\tilde{G}^2$. In Fig. 2(d) we plot the power, which increases monotonically with the decrease in frequency. In line with the work of [36], the Vakhitov-Kolokolov criterion about the sign of the derivative of P with $\tilde{\omega}$ here suggests the stability of the solitons.

Similarly, we write another key conserved quantity, the energy E, for Eq. (4) as

$$E = \int_{-\infty}^{\infty}\left(\psi_1^*\frac{\partial\psi_2}{\partial s} - \psi_2^*\frac{\partial\psi_1}{\partial s} + \frac{\tilde{M}}{2}(|\psi_1|^2 - |\psi_2|^2)\right.$$
$$\left. - \frac{1}{2}(|\psi_1|^4 + |\psi_2|^4)\right)\mathrm{d}s. \quad (30)$$

For the stationary soliton [Eq. (21)], the energy reduces to

$$E(\tilde{\omega}) = \sqrt{2}\tilde{M}\tanh^{-1}\left[\sqrt{\frac{1}{2}\left(1 - \frac{\tilde{\omega}^2}{\tilde{M}^2}\right)}\right]. \quad (31)$$

In Fig. 2(d) we observe that, as opposed to the power, the energy changes nonmonotonically as a function of frequency. However, it is important to point out that the energy maintains a definite sign and does not have a zero crossing. This is also

in line with the absence of instability according to the second criterion of the work of [36] in the context of Dirac equations. This criterion associates the zero crossings of the energy with a change of stability.

In summary, both stability criteria associated with nonlinear Dirac PDEs suggest the absence of instabilities for the localized waveforms examined herein. While, given the reduced nature of the NLD equation, the stability findings from these criteria are merely suggestive of the absence of a point spectrum (i.e., isolated linearization eigenvalue pair) instability for the breathing waveforms identified herein, we will see below that our numerical computations corroborate such findings. As an aside, we note that the translational invariance of the NLD PDE is tantamount to the conservation of linear momentum. However, since this latter conservation law is not directly related to the stability criteria of [36], we do not examine the latter in detail herein.

IV. SEMI-INFINITE CONTINUUM

Up to now our approach has been general in terms of obtaining localized solutions in the continuum approximation of the infinite lattice limit. We now seek decaying (edge) solutions for a semi-infinite domain $s \in [0, \infty)$. Recall that Eq. (20) was derived by imposing vanishing amplitudes only at $s \to \pm\infty$. Therefore, we can construct nonlinear edge solutions (finite at one edge and decaying as one moves farther away) with the same expression as given in Eq. (20) as long as $\theta(0)$ satisfies the given boundary condition at the edge.

Though any θ can be chosen at the boundary to obtain the corresponding edge solution, we are interested in some special cases, e.g., $\theta(0) = -\pi/2$ [$U(0) = 0$], $\theta(0) = 0$ [$U(0) = V(0)$], and $\theta(0) = \pi/2$ [$V(0) = 0$]. The physical meaning of such boundary conditions will be evident in the next section when we deal with a finite discrete chain. However, before moving further, we can reach some important conclusions.

We know that $\theta(s)$ varies spatially from $\theta(s) = -\cos^{-1}(\tilde{\omega}/\tilde{M})$ to $\theta(s) = \cos^{-1}(\tilde{\omega}/\tilde{M})$ in an infinite continuum [note the saddle points for Eqs. (14) and (15)]. Also, $\tilde{\omega} \in [-\tilde{M}, \tilde{M}]$ inside the band gap. Therefore, $\theta(s)$ in Eq. (20) obtained for an infinite chain will satisfy the boundary conditions $\theta(0) = -\pi/2$ [$U(0) = 0$] and $\theta(0) = \pi/2$ [$V(0) = 0$] only for $\tilde{\omega} \leqslant 0$, i.e., below the midgap frequency Ω_m. However, the boundary condition $\theta(0) = 0$ [$U(0) = V(0)$] will be satisfied for all $\tilde{\omega}$ inside the band gap.

A. Boundary with $\theta(0) = \pi/2$ [$V(0) = 0$]

For $\theta(0) = \pi/2$, Eq. (20) yields

$$s_0 = -\frac{1}{\sqrt{\tilde{M}^2 - \tilde{\omega}^2}}\tanh^{-1}\left(\sqrt{\frac{\tilde{M} + \tilde{\omega}}{\tilde{M} - \tilde{\omega}}}\right) \forall \tilde{\omega} \leqslant 0. \quad (32)$$

We observe that a nonzero s_0 simply means that we have a Dirac soliton which is moved to the $-s$ axis by a distance of s_0 $(=2\sqrt{2}z_0)$. We therefore get the edge solution for the domain $s \in [0, \infty)$. We calculate the corresponding power from Eq. (28) by changing the integration limits to account for the
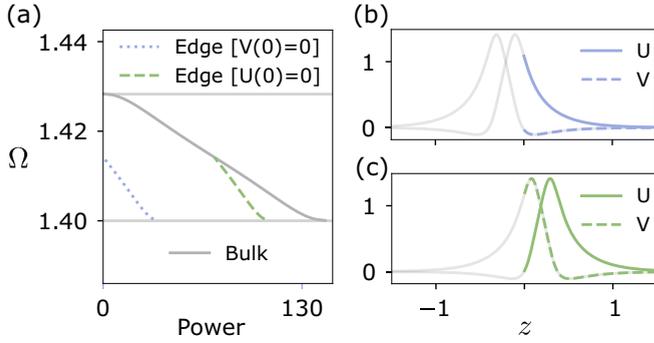
FIG. 3. Semi-infinite continuum NLD results. (a) Power of nonlinear edge states and Dirac solitons inside the band gap. (b) Edge state (nonlinearity modified) for the boundary with $\theta(0) = \pi/2$ $[V(0) = 0]$ at $\tilde{\omega} = -\tilde{M}/2$. The profile is a truncation of a shifted Dirac soliton (gray). (c) Edge state (nonlinearity induced) for the boundary with $\theta(0) = -\pi/2$ $[U(0) = 0]$ at $\tilde{\omega} = -\tilde{M}/2$. The profile is the other truncated part of a shifted Dirac soliton (gray).

finite boundary. In Fig. 3(a) we show the power as a function of frequency by a blue dashed line. Such edge solutions exist only for $\tilde{\omega} \leqslant 0$. In the linear limit with vanishing power, these solutions tend to $\tilde{\omega} = 0$, the midgap frequency. We show the Dirac soliton in gray in Fig. 3(b) for $\tilde{\omega} = -\tilde{M}/2$. Since the profile intersects $V = 0$ at a finite z for $\tilde{\omega} < 0$, nonlinear edge states can be considered a part of Dirac solitons, as shown in blue.

Interestingly, in the linear limit, the intersection of the soliton profile with $V = 0$ occurs at z (or s) $\rightarrow \infty$ for $\tilde{\omega} = 0$. From Eq. (21), we know for $\tilde{\omega} = 0$, we get $\theta \rightarrow \pi/4$ as $s \rightarrow \infty$. Therefore, from Eq. (14) we deduce that $\rho \propto \exp(-2\tilde{M}s)$, or in the NLD setting $[\psi_1, \psi_2] \propto \exp(-\tilde{M}s)$. This is the well-known Jackiw-Rebbi solution [18,46] in the linear Dirac framework; however, it is an edge solution, which is different from the standard interface solution between two media with different Dirac masses. We conclude that when nonlinearity is involved, this edge state is modified and a family of solutions is generated, as shown in blue in Fig. 3(a). We call them nonlinearity-modified edge states.

B. Boundary with $\theta(0) = -\pi/2$ $[U(0) = 0]$

Similarly, if we have $\theta(0) = -\pi/2$, Eq. (20) yields

$$s_0 = \frac{1}{\sqrt{\tilde{M}^2 - \tilde{\omega}^2}} \tanh^{-1}\left(\sqrt{\frac{\tilde{M} + \tilde{\omega}}{\tilde{M} - \tilde{\omega}}}\right) \forall \tilde{\omega} \leqslant 0. \quad (33)$$

This is equivalent to a Dirac soliton having moved to the $+s$ axis by a distance of s_0. In Fig. 3(a) we show the power as a function of frequency by a green dashed line. As discussed earlier, such edge solutions exist only for $\tilde{\omega} \leqslant 0$. At $\tilde{\omega} = 0$, these bifurcate from the Dirac soliton that lies in the bulk. Note that the bifurcation point corresponds to $s_0 \rightarrow \infty$. This means that the edge solution tends to the whole spatial profile of the Dirac soliton and therefore their powers tend to have the same value at the bifurcation point.

Contrary to the edge states discussed in the preceding section, the edge states, in this case, do not have any linear counterparts for vanishing power. Therefore, these sponta-

neously arise due to nonlinearity for $\tilde{\omega} \leqslant 0$. Figure 3(c) highlights the profile of such nonlinearity-induced edge states. These are reminiscent of nonlinear edge states found in diatomic lattices with two different masses [47].

Finally, we calculate the edge states for the boundary with $\theta(0) = 0$ $[U(0) = V(0)]$, which exist (the edge states) for the entire band gap (Appendix C). Again, these states are also nonlinearity-induced edge states with no linearized edge state at vanishing powers.

V. FINITE LATTICE

After analyzing the bulk and edge solutions in an infinite and a semi-infinite continuum, we now consider a finite discrete lattice and calculate nonlinear solutions inside the band gap. In addition, we investigate the instabilities that cause the localized solution to delocalize in space.

It is known that the FPUT lattice shown in Fig. 1(a) in its linear limit corresponds to a finite-frequency SSH chain [33]. Such a lattice supports topologically protected edge states in the case of fixed boundary conditions. However, this happens when the boundary is symmetry preserving, which physically means that it does not cut the unit cell. By contrast, a symmetry-breaking boundary, which cuts the unit cell, does not support an edge state [37]. It is at this point that we recognize the physical interpretation of specific boundary conditions that we chose in the preceding section. The boundary that supports a topological edge state in the linearized finite lattice resembles $V(0) = 0$ in the continuum limit. When nonlinearity is turned on, this edge state is referred to as a nonlinearity-modified edge state. Similarly, the boundary that does not support a topological edge state in the linearized finite lattice resembles $U(0) = 0$ in the continuum limit. However, when nonlinearity is turned on, we witness nonlinearity-induced edge states at finite power. In this section, we will show such edge states in the finite lattice and how they compare with their continuum counterparts.

A. Bifurcation diagrams

We take a lattice with 500 particles with fixed ends. The right boundary is kept free when obtaining edge solutions on the left edge. We use Newton's method to find the family of nonlinear periodic solutions for the lattice. By considering the linear edge state and the first state in the optical band as our initial guess, we are able to converge to the nonlinear solution and continue it over frequency. For the nonlinearity-induced edge states, however, this method does not work since there is no linear limit of such solutions. We tackle this by preparing the initial guess near the acoustic band by truncating the bulk solutions at $U \rightarrow 0$ as shown in Fig. 3(c). Note that we use symmetry-preserving boundaries in the finite lattice to obtain the nonlinearity-modified edge states. In contrast, symmetry-breaking boundaries are used to obtain the bulk and nonlinearity-induced edge states. In this way, we generate the bifurcation diagram for our discrete lattice as shown in Fig. 4(a). We observe a similar trend as predicted earlier in Fig. 3(a) with the existence of discrete breather analogs of the Dirac (bulk) solitons, nonlinearity-modified edge states, and nonlinearity-induced edge states.
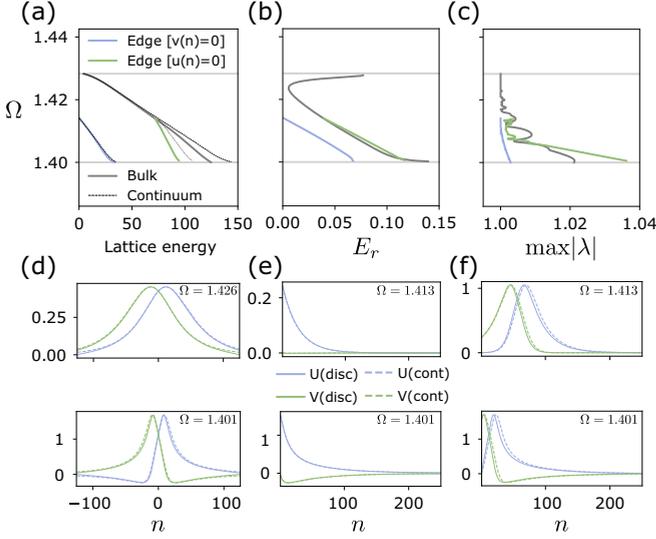
FIG. 4. Finite lattice results. (a) Bifurcation diagram obtained through the nonlinear continuation of the linear edge state (blue) and the first optical state (gray). In green is the nonlinearity-induced edge state. Their lattice energy is compared with the nonlinear states found for the continuum (dashed line). (b) Relative energy difference E_r between discrete and continuum solutions plotted inside the band gap for the bulk and edge solutions. (c) Maximum amplitude of the corresponding FMs indicating the extent of instability of discrete nonlinear solutions. (d) Comparison of bulk solutions at a frequency near the optical band ($\Omega = 1.426$) and acoustic band ($\Omega = 1.401$). (e) and (f) Comparison of (e) nonlinearity-modified and (f) nonlinearity-induced edge states, respectively, at a frequency near the midgap ($\Omega = 1.413$) and acoustic band ($\Omega = 1.401$).

To quantify the difference of lattice energy between the continuum model (E_{cont}) and the discrete model (E_{disc}), we define a relative energy parameter

$$E_r = (E_{\text{disc}} - E_{\text{cont}})/E_{\text{cont}}.$$

In Fig. 4(b) we show E_r as a function of frequency. We notice that $E_r \to 0$ for the nonlinearity modified edge state in its linear limit. This makes sense because $(\gamma, \Gamma) \approx O(\epsilon)$ and the zeroth-order dynamics is the linear limit at the midgap frequency Ω_m, where the edge state lies. For the bulk breather, E_r also decreases as it moves closer to the optical band. We observe a sudden rise in E_r very close to the optical band, which could be due to the decrease in localization of the bulk breather and its interaction with finite boundaries. In Figs. 4(d), 4(e), and 4(f) we show the comparison of discrete and continuum solutions for bulk breather, nonlinearity-modified edge state, and nonlinearity-induced edge state, respectively, at different frequencies inside the band gap. Overall, we observe an excellent match between discrete and continuum solutions, demonstrating that the finite lattice also supports the nonlinear solutions predicted by the nonlinear Dirac equations for $(\gamma, \Gamma) \approx O(\epsilon)$. We would like to highlight that at the bifurcation point (at the midgap), the edge state resembles the whole spatial profile of the Dirac soliton as discussed in the preceding section; therefore, their energies tend to be the same for the lattice.
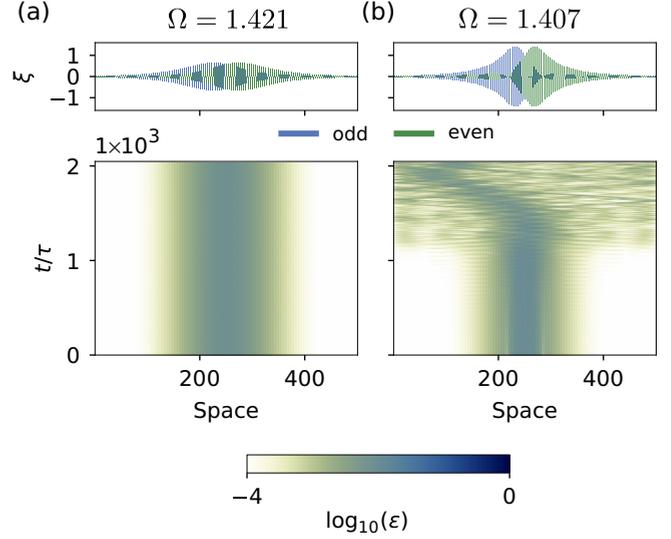

FIG. 5. Transient dynamics of discrete Dirac solitons in the finite lattice. (a) Soliton profile at $\Omega = 1.421$ (even and odd locations are highlighted with different colors) and the transient dynamics when the profile is given as the initial condition to the lattice. The colormap shows the energy density. (b) Same as (a) but for the soliton at $\Omega = 1.407$, which has a larger FM. The soliton delocalizes due to the presence of instabilities.

We then perform linear stability analysis of the nonlinear solutions of the finite lattice using Floquet theory [27]. In Fig. 4(c) we plot the maximum amplitude of the Floquet multipliers (FMs) corresponding to the nonlinear states inside the band gap. Recall that the values of the FMs that are larger than unity (in absolute value) imply the existence of instabilities. We observe that the Dirac soliton remains linearly stable for higher frequencies, near the optical band. However, it becomes generally unstable with the increase in lattice energy at low frequencies. Such instabilities emerge due to the finite size of the lattice, are associated with quartets of FMs with modulus larger than unity, and are expected to vanish for large lattices (see Appendix D for more details). This is in line with the fact observed previously (when calculating the conserved quantities at the continuum level) that none of the criteria for the emergence of (in that case, real FM-associated) instabilities of [36] were met in this context. Similarly, we also observe that both types of edge states become unstable with the increase in lattice energy. In particular, nonlinearity-induced edge states are more unstable compared to nonlinearity-modified edge states. However, in both cases, once again the instabilities (that are progressively featuring higher growth rates as the acoustic band is approached) are associated with complex FM quartets, i.e., they are oscillatory in nature (see also [33]).

B. Transient dynamics of discrete Dirac solitons and edge states

We now present the transient dynamics of our discrete analogs of the continuum Dirac solitons and also of the edge states. In Fig. 5(a) we show a discrete Dirac soliton at $\Omega = 1.421$, which is linearly stable. We apply 1% noise to its profile and provide the resulting profile as an initial condition
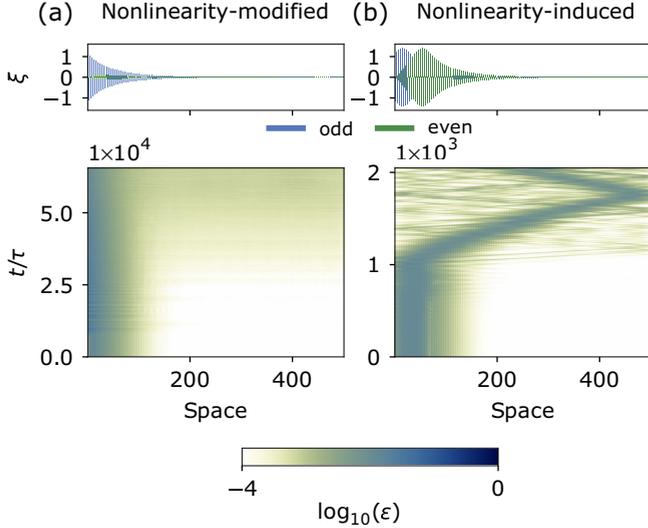
FIG. 6. Transient dynamics of edge states in the finite lattice. (a) Nonlinearity-modified edge state at $\Omega = 1.407$. The transient dynamics shows that the edge state loses its energy to the bulk due to instabilities. (b) Nonlinearity-induced edge state profile and its dynamics at $\Omega = 1.407$. Its transient dynamics shows a stronger delocalization in the form of a robust wave packet moving in the bulk.

to our finite lattice for a simulation time of $2000\tau_0$, where τ_0 is the time period of the nonlinear state. We plot the energy density ε for each mass that includes its kinetic energy and the mean of the potential energy of its left and right neighboring springs such that

$$\varepsilon_i = \frac{\frac{1}{2}\dot{\xi}_i^2 + \frac{1}{2}[E_{\text{pot}}(\xi_{i-1}, \xi_i) + E_{\text{pot}}(\xi_i, \xi_{i+1})]}{\sum_{i=1}^{N}\left\{\frac{1}{2}\dot{\xi}_i^2 + \frac{1}{2}[E_{\text{pot}}(\xi_{i-1}, \xi_i) + E_{\text{pot}}(\xi_i, \xi_{i+1})]\right\}}, \quad (34)$$

where $E_{\text{pot}}(\xi_i, \xi_{i+1}) = \frac{1}{2}(1 \pm \gamma)(\xi_i - \xi_{i+1})^2 + \frac{1}{4}\Gamma(\xi_i - \xi_{i+1})^4$. The plus and minus signs alternate for adjacent pairs of nearest neighbors in line with Eq. (1). We observe that the discrete Dirac soliton remains localized, confirming its linear stability. In Fig. 5(b) we show a discrete Dirac soliton at $\Omega = 1.407$, which is linearly unstable through the FM quartets discussed above. Contrary to the previous case, the Dirac soliton starts shedding its energy at around $1200\tau_0$. Interestingly, a localized traveling wave packet is observed as a consequence. Exploring the question of potentially genuine traveling such states is an interesting question for future work, as we also highlight below in Sec. VI.

Finally, we examine the transient dynamics of nonlinear edge states. In Fig. 6(a) we show a nonlinearity-modified edge state at $\Omega = 1.407$, which is linearly unstable. Recall that a topological edge state exists for this lattice in the linear limit. Transient simulations reveal that the localized mode starts shedding its energy to the bulk gradually while degenerating toward the corresponding linear state. In Fig. 6(b) we show a nonlinearity-induced edge state at the same frequency. Recall that no such topological edge state exists for this lattice in the linear limit. Since this nonlinear state is also linearly unstable, the transient simulations reveal that the edge state sheds its energy. However, different from the nonlinearity-modified

edge dynamics and similar to the dynamics of the unstable discrete Dirac soliton in Fig. 5(b), the edge state delocalization is accompanied by a localized wave that travels in the bulk. A similar phenomenon was also reported recently in a nonlinear SSH model of photonics [32]. We conjecture that these belong to lower-energy and higher-frequency soliton solutions near the optical band, which is a feature worth exploring further.

VI. CONCLUSION

In the present work, we have examined an SSH-type linear (dimer) system in the presence of an intersite nonlinearity of the β-FPUT type. We have leveraged our ability to control the linear band via a small parameter to develop a formal expansion in the vicinity of the band edge of the system. This in turn led us to a variant of the nonlinear Dirac equations. We used a sequence of linear and subsequently nonlinear (using polar coordinates) transformations to rewrite the relevant equations of motion. We observed that the equations simplify considerably in the limit of seeking the stationary nonlinear (continuum) wave. Eventually, the relevant coupled ODE problem not only is amenable to phase plane analysis, but it can also provide the soliton solution in closed analytical form. This in turn permits the computation of the associated conserved quantities (also discussed herein) "at" the solitonic solution. Armed with the knowledge of the coherent analytical structure, we then studied semi-infinite and finite-domain problems. We were able to show that a suitable adaptation of the soliton can be made to comply with concrete boundary conditions. This was sufficient (based on the bulk-boundary correspondence) to express the finite and semi-infinite domain edge states. We witnessed not only nonlinearity-modified topological edge states but also nonlinearity-induced edge states with no linear counterpart. The latter bifurcate from the bulk soliton solutions. We also examined the stability of the solitons and found that the deeper one goes into the gap, the more unstable the solutions. However, these instabilities were of an oscillatory type and tended to be weaker for large lattices, suggesting the stabilization in the infinite lattice limit. When the instability dynamics was explored, typically we saw that a solitonlike wave was led to move within the lattice.

Naturally, this is only an initial step towards the more systematic study of the lattices considered herein. One can envision numerous additional topics for future research. For instance, in the present work we have limited our considerations to single stationary solitons. However, when instabilities arose, they often seemed to give rise to some propagating patterns spontaneously. It would be interesting to explore further whether such genuinely traveling structures exist (even if for isolated parameter values as in, e.g., the mass-dimer granular variant of [48]) or not. It is interesting to point out in this context that should such traveling wave solutions exist, the consideration of their momentum as a function of their speed would be worthwhile to consider in connection to their stability, in line with classic studies along this vein, e.g., in [49]. Furthermore, while we have constrained considerations to one-dimensional settings, generalizations to 2D lattices would be particularly interesting. This is due, among other things, to the fact that 2D nonlinear Dirac equations have been argued to have not only similarities to but also intriguing differences

from their NLS counterparts [50]. This is both in terms of the stability of solitons and connection to the existence of vortical patterns.

ACKNOWLEDGMENTS

APPENDIX A: CONTINUUM VS DISCRETE DISPERSION

Here we verify that the dispersion relation in the continuum, as described by the PDEs (3), captures fairly well the dispersion relation characterizing the discrete system given by Eq. (1). By substituting plane-wave solutions $u(z) = u_0 \exp[i(\tilde{q}_c z - \tilde{\omega}_c \tau)]$ and $v(z) = v_0 \exp[i(\tilde{q}_c z - \tilde{\omega}_c \tau)]$ in the linearized ($\tilde{\Gamma} = 0$) Eq. (3), we get the dispersion relation for the continuum as

$$\tilde{\omega}_c = \pm\sqrt{\tilde{M}^2 + \tilde{q}_c^2/8}. \tag{A1}$$

Since this dispersion relation holds for the scaled coordinates, i.e., $z = \epsilon n$ and $\tau = \epsilon t$, an equivalent dispersion relation in the original coordinates (n, t) would be

$$\omega_c = \pm\sqrt{M^2 + q_c^2/8}, \tag{A2}$$

where $\omega_c = \epsilon\tilde{\omega}_c$, $q_c = \epsilon\tilde{q}_c$, and $M = \epsilon\tilde{M}$. Similarly, we calculate the dispersion of the discrete system in Eq. (1) as

$$\omega_d = \sqrt{2 + \sqrt{(1 - \gamma)^2 + (1 + \gamma)^2 + 2(1 - \gamma^2)\cos q_d}}. \tag{A3}$$

When using the ansatz in Eq. (2), we know that plane-wave parameters are related as $q_d = |\pi + q_c|$ and $\omega_d = |\Omega + \omega_c|$. This means that the dispersion curve for the discrete chain in Eq. (37) has to be shifted in wave number and frequency to be compared to the dispersion in Eq. (36). We compare the two in Fig. 7 and find a good match for the small-band-gap case of interest herein.
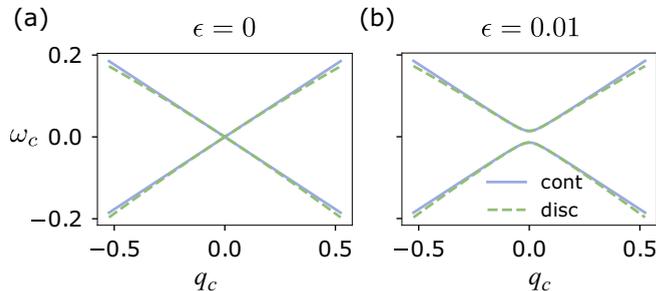

FIG. 7. Comparison of continuum (solid line) and discrete dispersion (dashed line) for (a) $\epsilon = 0$ and (b) $\epsilon = 0.01$ with $\tilde{\gamma} = 2$.
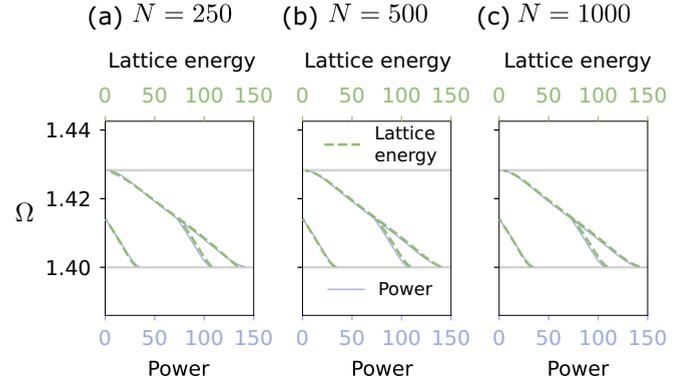

FIG. 8. Comparison of NLD power and lattice energy for Dirac solitons and edge states in continuum. Three different lattice sizes are taken: (a) $N = 250$, (b) $N = 500$, and (c) $N = 1000$.

APPENDIX B: ENERGY OF THE LATTICE VS THE POWER OF NLD EQUATIONS

For nonlinear periodic solutions (standing wave) at frequency $\Omega = \Omega_m + \epsilon\tilde{\omega}$, let $|\xi|$ denote the amplitude of oscillations. We can then write the total energy of the lattice as the maximum potential energy

$$
\begin{aligned}
E_{\text{lattice}}(\tilde{\omega}) = \sum_{\text{unit cells } n} \Bigg[&\frac{1}{4}(1 + \gamma)(|\xi|_{2,n-1} - |\xi|_{1,n})^2 \\
&+ \frac{1}{8}\Gamma(|\xi|_{2,n-1} - |\xi|_{1,n})^4 \\
&+ \frac{1}{2}(1 - \gamma)(|\xi|_{1,n} - |\xi|_{2,n})^2 \\
&+ \frac{1}{4}\Gamma(|\xi|_{1,n} - |\xi|_{2,n})^4 \\
&+ \frac{1}{4}(1 + \gamma)(|\xi|_{2,n} - |\xi|_{1,n+1})^2 \\
&+ \frac{1}{8}\Gamma(|\xi|_{2,n} - |\xi|_{1,n+1})^4 \Bigg].
\end{aligned} \tag{B1}
$$

We then follow the same procedure described in Sec. III and employ a continuum approximation to reduce the equation in terms of the amplitude of ψ_1 and ψ_2 such that

$$E_{\text{lattice}}(\tilde{\omega}) = \int_{-\infty}^{\infty} \left(\frac{1}{4G^2\sqrt{2}}(|\psi_1|^2 + |\psi_2|^2) + \cdots \right) ds, \tag{B2}$$

where $G = \sqrt{-3\Gamma/4\sqrt{2}}$ and the dots denote higher-order terms. This equation is tantamount to the power of the NLD equation (28) for small $|\psi_1|$ and $|\psi_2|$. In Fig. 8 we show the comparison of lattice energy and power for Dirac solitons and edge states that were found analytically for a continuum, illustrating the very good agreement between the two.

APPENDIX C: BOUNDARY WITH $\theta(0) = 0$ [$U(0) = V(0)$]

For $\theta(0) = 0$, Eq. (20) yields $s_0 = 0$. Interestingly, this results in exactly the same profile as that of Dirac soliton; however, we take the right half for the semi-infinite domain
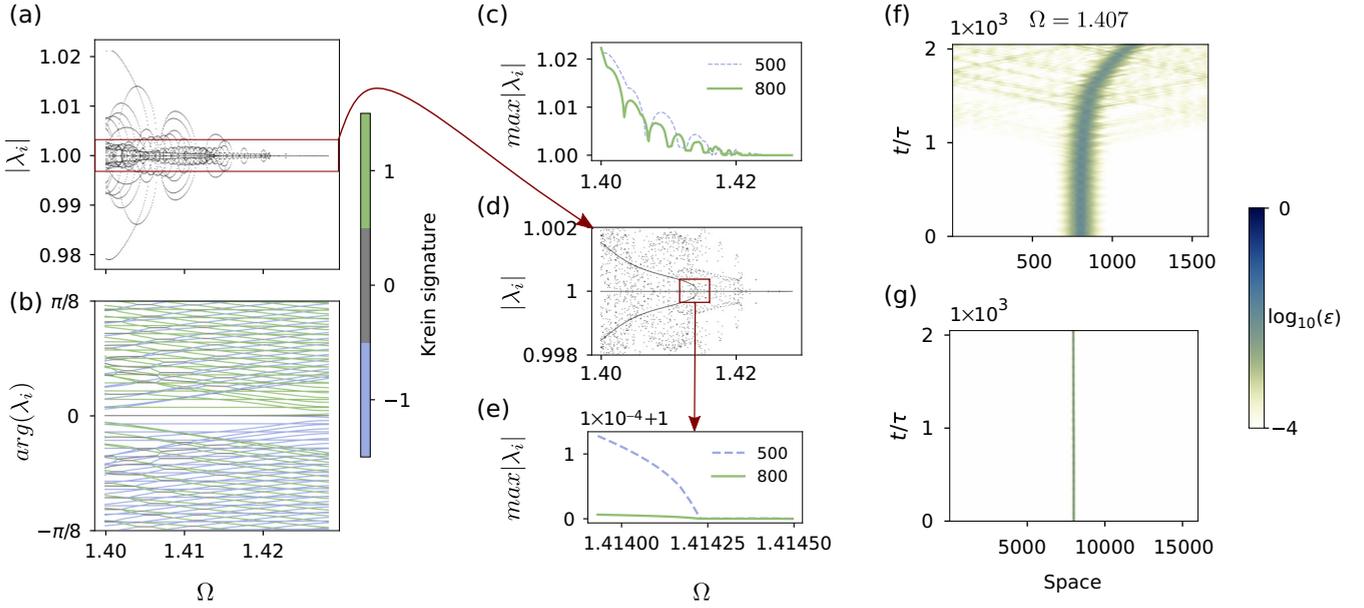
FIG. 9. Stability of discrete Dirac soliton. (a) FM amplitude as a function of frequency inside the band gap for Dirac solitons. (b) Same as (a) but for the FM phase. Colors denote the Krein signature of Floquet eigenmode. (c) FM amplitude decreases as the lattice length is increased, indicating the existence of finite-size instabilities. (d) Zoomed-in view of (a), indicating the emergence of a peculiar instability at the midgap frequency $\Omega_m = \sqrt{2}$. (e) This instability drastically diminishes with the increase in lattice length. (f) Spatial-temporal dynamics of the Dirac soliton at $\Omega = 1.407$ in a large lattice of $N = 1500$. (g) Same as (f) but for an even larger lattice of $N = 15\,000$. The colormap shows the energy density.

$s \in [0, \infty)$. Since the Dirac soliton exists for the entire band gap, this edge state also exists for the entire band gap, i.e., $\tilde{\omega} \in [-\tilde{M}, \tilde{M}]$. For the finite chain, this case corresponds to a free end instead of a fixed one.

APPENDIX D: TYPES OF INSTABILITIES

Here we examine the instabilities of discrete Dirac solitons in more detail. In Figs. 9(a) and 9(b) we show the amplitude and phase of FM for solitons inside the band gap. We observe that solitons become unstable, i.e., $|\lambda_i| > 1$, for most of the frequencies below $\Omega = 1.42$. Krein signature analysis [33] reveals that such instabilities are due to the collision of bulk spectrum in Fig. 9(b). Therefore, these are bulk-bulk or finite-size instabilities [33]. In Fig. 9(c) we show that such instabilities reduce with the increase of lattice

size. This makes sense due to the existence of finite-size instabilities. In Fig. 9(d) we highlight the instability that emerges at the midgap frequency $\Omega = \sqrt{2}$. This instability is a result of coupling between the discrete Dirac soliton and the nonlinearity-induced edge state. As the length of the lattice is increased, this coupling is reduced and thus the instability drastically diminishes as shown in Fig. 9(e). We further confirm this by performing transient simulations on large lattices. We give the analytically obtained Dirac soliton solution at $\Omega = 1.407$ as an initial condition to large lattices of size $N = 1500$ and $15\,000$ in Figs. 9(f) and 9(g), respectively. We observe stable propagation of the breathing soliton in the larger lattice over the course of the monitored time horizon, indicating the reduction of finite-size instabilities in such lattices.

[1] E. Fermi, J. Pasta, S. Ulam, and M. Tsingou, Studies of the nonlinear problems, Tech. Rep. No. LA-1940 (Los Alamos National Laboratory, 1955).

[2] G. Gallavotti, *The Fermi–Pasta–Ulam Problem: A Status Report* (Springer, Berlin, 2008).

[3] M. Porter, N. Zabusky, B. Hu, and D. Campbell, Fermi, Pasta, Ulam and the birth of experimental mathematics, Am. Sci. **97**, 214 (2009).

[4] V. F. Nesterenko, *Dynamics of Heterogeneous Materials* (Springer, Heidelberg, 2001).

[5] C. Chong, M. A. Porter, P. G. Kevrekidis, and C. Daraio, Nonlinear coherent structures in granular crystals, J. Phys.: Condens. Matter **29**, 413003 (2017).

[6] Y. Starosvetsky, K. R. Jayaprakash, M. A. Hasan, and A. F. Vakakis, *Topics on the Nonlinear Dynamics and Acoustics of Ordered Granular Media* (World Scientific, Singapore, 2017).

[7] G. Theocharis, N. Boechler, and C. Daraio, *Nonlinear Periodic Phononic Structures and Granular Crystals* (Springer, Berlin, 2013), pp. 217–251.

[8] A. Mehrem, N. Jiménez, L. J. Salmerón-Contreras, X. García-Andrés, L. M. García-Raffi, R. Picó, and V. J. Sánchez-Morcillo, Nonlinear dispersive waves in repulsive lattices, Phys. Rev. E **96**, 012208 (2017).

[9] C. Chong, Y. Wang, D. Maréchal, E. G. Charalampidis, M. Molerón, A. J. Martínez, M. A. Porter, P. G. Kevrekidis, and C. Daraio, Nonlinear localized modes in two-dimensional

hexagonally-packed magnetic lattices, New J. Phys. **23**, 043008 (2021).

[10] H. Yasuda, Y. Miyazawa, E. G. Charalampidis, C. Chong, P. G. Kevrekidis, and J. Yang, Origami-based impact mitigation via rarefaction solitary wave creation, Sci. Adv. **5**, eaau2835 (2019).

[11] L. H. Haddad and L. D. Carr, The nonlinear Dirac equation in Bose–Einstein condensates: Foundation and symmetries, Physica D **238**, 1413 (2009).

[12] L. H. Haddad and L. D. Carr, The nonlinear Dirac equation in Bose–Einstein condensates: Vortex solutions and spectra in a weak harmonic trap, New J. Phys. **17**, 113011 (2015).

[13] M. J. Ablowitz, S. D. Nixon, and Y. Zhu, Conical diffraction in honeycomb lattices, Phys. Rev. A **79**, 053830 (2009).

[14] M. J. Ablowitz and Y. Zhu, Evolution of Bloch-mode envelopes in two-dimensional generalized honeycomb lattices, Phys. Rev. A **82**, 013840 (2010).

[15] J. Cuevas-Maraver, N. Boussaïd, A. Comech, R. Lan, P. G. Kevrekidis, and A. Saxena, in *Nonlinear Systems*, edited by V. Carmona, J. Cuevas-Maraver, F. Fernández-Sánchez, and E. García-Medina (Springer International, Cham, 2018), Vol. 1, pp. 89–143.

[16] N. Boussaïd and A. Comech, *Nonlinear Dirac Equation: Spectral Stability of Solitary Waves* (American Mathematical Society, Providence, 2019).

[17] M. Z. Hasan and C. L. Kane, *Colloquium*: Topological insulators, Rev. Mod. Phys. **82**, 3045 (2010).

[18] N. R. Cooper, J. Dalibard, and I. B. Spielman, Topological bands for ultracold atoms, Rev. Mod. Phys. **91**, 015005 (2019).

[19] T. Ozawa, H. M. Price, A. Amo, N. Goldman, M. Hafezi, L. Lu, M. C. Rechtsman, D. Schuster, J. Simon, O. Zilberberg, and I. Carusotto, Topological photonics, Rev. Mod. Phys. **91**, 015006 (2019).

[20] R. Süsstrunk and S. D. Huber, Classification of topological phonons in linear mechanical metamaterials, Proc. Natl. Acad. Sci. USA **113**, E4767 (2016).

[21] G. Ma, M. Xiao, and C. T. Chan, Topological phases in acoustic and mechanical systems, Nat. Rev. Phys. **1**, 281 (2019).

[22] B. A. Bernevig and T. L. Hughes, *Topological Insulators and Topological Superconductors* (Princeton University Press, Princeton, 2013).

[23] C. L. Kane and E. J. Mele, Quantum spin Hall effect in graphene, Phys. Rev. Lett. **95**, 226801 (2005).

[24] X. Wan, A. M. Turner, A. Vishwanath, and S. Y. Savrasov, Topological semimetal and Fermi-arc surface states in the electronic structure of pyrochlore iridates, Phys. Rev. B **83**, 205101 (2011).

[25] W. A. Benalcazar, B. A. Bernevig, and T. L. Hughes, Quantized electric multipole insulators, Science **357**, 61 (2017).

[26] S. Flach and A. V. Gorbach, Discrete breathers — Advances in theory and applications, Phys. Rep. **467**, 1 (2008).

[27] S. Aubry, Discrete breathers: Localization and transfer of energy in one-dimensional Hamiltonian nonlinear systems, Physica D **216**, 1 (2006).

[28] R. Livi, M. Spicci, and R. S. MacKay, Breathers on a diatomic FPU chain, Nonlinearity **10**, 1421 (1997).

[29] P. Maniadis, A. V. Zolotaryuk, and G. P. Tsironis, Existence and stability of discrete gap breathers in a di-

atomic β Fermi-Pasta-Ulam chain, Phys. Rev. E **67**, 046612 (2003).

[30] G. James and P. Noble, Breathers on diatomic Fermi–Pasta–Ulam lattices, Physica D **196**, 124 (2004).

[31] W. P. Su, J. R. Schrieffer, and A. J. Heeger, Solitons in polyacetylene, Phys. Rev. Lett. **42**, 1698 (1979).

[32] Y.-P. Ma and H. Susanto, Topological edge solitons and their stability in a nonlinear Su-Schrieffer-Heeger model, Phys. Rev. E **104**, 054206 (2021).

[33] R. Chaunsali, H. Xu, J. Yang, P. G. Kevrekidis, and G. Theocharis, Stability of topological edge states under strong nonlinear effects, Phys. Rev. B **103**, 024106 (2021).

[34] A. Hofstrand, H. Li, and M. I. Weinstein, Discrete breathers of nonlinear dimer lattices: Bridging the anti-continuous and continuous limits, J. Nonlinear Sci. **33**, 59 (2023).

[35] D. A. Smirnova, L. A. Smirnov, D. Leykam, and Y. S. Kivshar, Topological edge states and gap solitons in the nonlinear Dirac model, Laser Photon. Rev. **13**, 1900223 (2019).

[36] G. Berkolaiko, A. Comech, and A. Sukhtayev, Vakhitov–Kolokolov and energy vanishing conditions for linear instability of solitary waves in models of classical self-interacting spinor fields, Nonlinearity **28**, 577 (2015).

[37] R. Chaunsali and G. Theocharis, Self-induced topological transition in phononic crystals by nonlinearity management, Phys. Rev. B **100**, 014302 (2019).

[38] Y. S. Kivshar, Class of localized structures in nonlinear lattices, Phys. Rev. B **46**, 8652 (1992).

[39] O. A. Chubykalo, A. S. Kovalev, and O. V. Usatenko, Dynamical solitons in a one-dimensional nonlinear diatomic chain, Phys. Rev. B **47**, 3153 (1993).

[40] N. Alexeeva, I. Barashenkov, and A. Saxena, Spinor solitons and their $\mathcal{PT}$-symmetric offspring, Ann. Phys. (NY) **403**, 198 (2019).

[41] G. Huang and B. Hu, Asymmetric gap soliton modes in diatomic lattices with cubic and quartic nonlinearity, Phys. Rev. B **57**, 5746 (1998).

[42] B. Hu, G. Huang, and M. G. Velarde, Dynamics of coupled gap solitons in diatomic lattices with cubic and quartic nonlinearities, Phys. Rev. E **62**, 2827 (2000).

[43] D. L. Mills and S. E. Trullinger, Gap solitons in nonlinear periodic structures, Phys. Rev. B **36**, 947 (1987).

[44] A. Aceves and S. Wabnitz, Self-induced transparency solitons in nonlinear refractive periodic media, Phys. Lett. A **141**, 37 (1989).

[45] D. N. Christodoulides and R. I. Joseph, Slow Bragg solitons in nonlinear periodic structures, Phys. Rev. Lett. **62**, 1746 (1989).

[46] R. Jackiw and C. Rebbi, Solitons with fermion number 1/2, Phys. Rev. D **13**, 3398 (1976).

[47] Y. S. Kivshar, Nonlinear surface modes in monoatomic and diatomic lattices, Physica D **113**, 248 (1998).

[48] K. R. Jayaprakash, Y. Starosvetsky, and A. F. Vakakis, New family of solitary waves in granular dimer chains with no precompression, Phys. Rev. E **83**, 036606 (2011).

[49] I. V. Barashenkov, Stability criterion for dark solitons, Phys. Rev. Lett. **77**, 1193 (1996).

[50] J. Cuevas–Maraver, P. G. Kevrekidis, A. Saxena, A. Comech, and R. Lan, Stability of solitary waves and vortices in a 2D nonlinear Dirac model, Phys. Rev. Lett. **116**, 214101 (2016).